Spatiotemporal variability and front-locked circulation of salinity fronts in Hangzhou Bay

Jiawei Zhang[a], Jingui Liu [abcd*], Shuo Li[a], Shunqi Pan[d]

[a]Guangdong Key Laboratory for Coastal Ocean Variation and Disaster Prediction, Guangdong Ocean University (GDOU), Zhanjiang, 524088, China

[b]Key Laboratory of Marine Spatial Resource Management Technology, Ministry of Natural Resources, Hangzhou, 310005, China

[c]Shelf and Deep-sea Climate, Resources, and Environment Key Laboratory of Guangdong Province for General Universities, GDOU, Zhanjiang, 524088, China

[d]School of Engineering, Cardiff University, Cardiff, CF24 3AA, UK

*Corresponding author. Guangdong Key Laboratory for Coastal Ocean Variation and Disaster Prediction, Guangdong Ocean University (GDOU), Zhanjiang, 524088, China.

E-mail address: jinguiliu1981@hotmail.com (J. Liu).

Abstract

Estuarine salinity fronts significantly regulate circulation, sediment dynamics, and pollutant transport in coastal systems. In Hangzhou Bay, a persistent northeast-southwest salinity front has been observed; however, its three-dimensional structure and dynamical maintenance remain poorly constrained, particularly under climate change conditions and intensifying anthropogenic pressures. Here, a high-resolution three-dimensional hydrodynamic model based on the Finite-Volume Community Ocean Model is developed to investigate the formation, variability, and governing dynamics of salinity fronts in Hangzhou Bay. Results show pronounced spatiotemporal variability in frontal intensity across seasonal and tidal scales. Surface frontal intensity peaks during wet-season neap tides, driven by enhanced salinity stratification and reduced tidal mixing, whereas dry-season variability is primarily modulated by strong northerly winds and associated Ekman transport. A clear spatial asymmetry in frontal structure is identified across the bay: north of the bay mouth, the water column remains well mixed, producing a predominantly vertical frontal structure. In contrast, the southern bay displays partially mixed to stratified conditions, forming inclined fronts, with the strongest salinity stratification occurring during wet-season neap tide. Within the frontal zone, coherent front-locked circulation develops as single and double clockwise circulation, accompanied by vertical velocities on the order of 10^{-6}-10^{-5} m/s. Surface residual currents are generally stronger than bottom currents, which are significantly attenuated near the front due to bottom friction and the Coriolis effects. Momentum diagnostics demonstrate that this frontal system is maintained by a frictionally modified baroclinic balance, with wind forcing as a secondary modulator. This study provides a process-based framework applicable to other macrotidal estuarine systems.

Keywords: Hangzhou Bay; Salinity Front; Three-Dimensional Structure; FVCOM; Spatiotemporal Variation

1. Introduction

Estuaries are highly dynamic and complex coastal systems shaped by the interaction between tidal forcing and terrestrial freshwater input. Their hydrodynamic regimes are governed by multiple processes, including tides, river discharge, winds, and coastal circulation, often exhibiting funnel-shaped and semi-enclosed morphologies (Scanes et al., 2017; Cardoso, 2022). Within such environments, sharp gradients in hydrographic properties frequently emerge, giving rise to frontal systems that play a central role in estuarine dynamics.

The concept of fronts was originally developed in meteorology and later introduced into oceanography to describe banded regions characterized by rapid changes in surface density (Cromwell and Reid, 1956). Since the 1990s, growing attention has been paid to estuarine and bay fronts, particularly their roles in regulating circulation, material transport, and ecosystem functioning. In estuarine environments, the interaction between freshwater outflows and offshore seawater generates strong horizontal and vertical gradients in salinity, temperature, and density, forming salinity fronts that organize local circulation and exchange processes. These fronts are known to enhance biological productivity (Belkin et al., 2009; Miller and Christodoulou, 2014), control sediment transport and deposition (Wang et al., 2024), influence pollutant accumulation and dispersion (Wang et al., 2022), and facilitate air-sea interactions through mechanisms such as frontal circulation, water convergence, and vertical mixing; through these processes, they facilitate the exchange of vital substances including oxygen, heat, and carbon across the mixed layer (Ferrari, 2011).

China's coastal waters host a wide variety of frontal systems driven by the convergence of the Kuroshio Warm Current, coastal upwelling, and freshwater dilution (Hickox et al., 2000). Within this broader context, estuarine salinity fronts along the Chinese coast have attracted considerable attention due to their role in sediment transport, pollutant dispersion, and cross-frontal material exchange (Ning et al., 2004; Liu et al., 2022; Tian et al., 2025). Nevertheless, because frontal structure and dynamics are strongly modulated by local bathymetry, tidal regime, and runoff variability, their spatiotemporal evolution and dynamical maintenance remain highly system-dependent and are not yet fully understood in macrotidal settings.

Hangzhou Bay (HZB), the largest trumpet-shaped bay in China, exemplifies a typical macrotidal estuary dominated by regular semidiurnal tides (Li et al., 2022). Geographically, its northern shore borders the Yangtze River Estuary (YRE), with the western boundary connected to the Qiantang River (QTR). Its eastern side opens into the Zhoushan Archipelago and the East China Sea. A persistent northeast-southwest (NE-SW) oriented front exists year-round within the bay, which can be further subdivided into the QTR plume front and the secondary Yangtze River (YR) plume front. The morphology, vertical structure, and spatial position of this frontal system are jointly controlled by multiple dynamic factors, including the discharges of the YR and QTR, tidal forcing, and coastal winds (Su, 1992; Du et al., 2010; Wang et al., 2013). In terms of ecological effects, the dynamic processes associated with the frontal system exert multiple regulatory functions on the estuarine ecosystem. Upwelling induced by frontal convergence, along with frontal circulation and its inherent instabilities, can significantly influence the transport processes of benthic nutrients (Lohmann and Belkin, 2014; Lévy et al., 2018). Meanwhile, shifts in frontal position further modulate the spatial distribution patterns of planktonic communities within the bay (Xu et al., 2024). In addition, this frontal system also exerts a notable influence on bacterial abundance in the waters of Hangzhou Bay, thereby serving, to a certain extent, as an indicator of the dynamic status of water quality in the bay (Su, 1992).

Despite decades of observational research, previous work on the HZB salinity front relied on transect observations since the 1990s and two-dimensional models (Huang, 1993), leaving the three-dimensional structure, the stratification-circulation coupling, the maintaining momentum balance, and the relative roles of tidal mixing and wind forcing insufficiently quantified. To address these knowledge gaps, this study develops a high-resolution, three-dimensional hydrodynamic model of the HZB based on Finite-Volume Community Ocean Model (FVCOM). Using model simulations under contrasting seasonal (wet and dry) and tidal (spring and neap) conditions, we investigate the spatiotemporal variability of the salinity front, its vertical structure and stratification control, and the associated front-locked circulation. Through momentum diagnostics and wind forcing analysis, we further elucidate the primary dynamical balance governing the frontal system and the secondary modulation by wind-driven processes. By integrating these results, this study aims to establish a process-based understanding of salinity front dynamics in the HZB and to provide a conceptual framework applicable to other macrotidal estuarine systems.

2. Model and methods

2.1. Model setup

A three-dimensional hydrodynamic model of the HZB was constructed using the Finite-Volume Community Ocean Model (FVCOM) (Chen et al., 2006). The model domain encompasses the Fuchunjiang Dam in the upper reaches of the QTR, Jiangyin in the upper reaches of the YR, and a portion of the East China Sea shelf, spanning longitude of 119.6°E-124.5°E and latitude of 28.3°N-34.3°N (Fig. 1). To better fit the complex coastline and irregular bathymetry of the region, an unstructured triangular grid was employed, consisting of 79,107 nodes and 152,461 elements. The HZB, as the focal estuarine region characterized by shallow water depths, was locally refined to ensure computational accuracy. The horizontal grid resolution across the entire domain, covering the region from the upstream river channels to the offshore open boundary, ranges from 0.04 km to 15.0 km. The vertical coordinate system was discretized into 20 uniform sigma layers extending from the sea surface to the seabed.

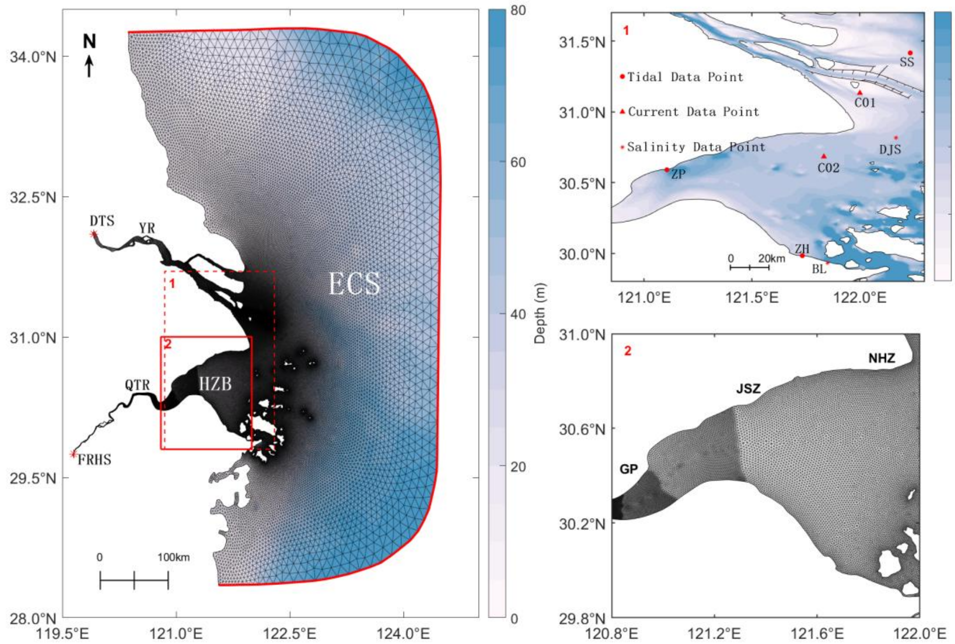

Fig. 1. Survey stations and unstructured mesh grid in the HZB. The outer red curve denotes the open boundary. Abbreviations: HZB, Hangzhou Bay; FRHS, Fuchunjiang Hydropower Station; DTS, Datong Station; QTR, Qiantang River; YR, Yangtze River; ZP, ZhaPu; ZH, ZhenHai; SS, SheShan; GP, GanPu; BL, BeiLun; DJS, Dajishan; JSZ, Jinshanzui; NHZ, Nanhuizui; ECS, the East China Sea; C01 and C02 correspond to current data point 1 and 2, respectively. Area 1 marks the location of observational stations; Area 2 outlines the computational domain of the HZB grid.

The model utilized a mode-splitting algorithm with an external time step of 0.3 s and an internal-to-external time step ratio of 6. A minimum depth of 0.05 m was prescribed for the wetting and drying scheme. Grids with water depth below this threshold were defined as dry grids and excluded from calculations. Bathymetric data for the East China Sea were obtained from the ETOPO1 dataset (https://www.ngdc.noaa.gov/mgg/global/global.html), while bathymetry for the HZB, Fuchunjiang, and YR was refined using nautical bathymetry charts. Surface forcing data were provided by the ERA5 reanalysis dataset (ECMWF, https://www.ecmwf.int/), including 10-m wind fields, precipitation, relative humidity, and longwave and shortwave radiation fluxes. This dataset has a temporal resolution of 1 hour and a horizontal resolution of 0.25°×0.25°. The initial salinity fields and open boundary conditions were derived from the GLORYS global reanalysis (hourly fields, horizontal resolution of 1/12°×1/12°). The tidal boundary conditions were prescribed using the amplitudes and phases of eight major tidal constituents (M_2, S_2, K_2, N_2, K_1, O_1, P_1, Q_1) from the global TPXO tidal dataset. The river discharge used in the model was derived from observations at the Datong Station of the YR and the Fuchunjiang Hydropower Station. The data had a daily temporal resolution (Fig. 2), with salinity set to zero. The simulation period extended from 1 January to 31 December 2021; July and December were selected as representative of the wet and dry seasons (wet-season spring tide: 12 July; neap tide: 19 July; dry-season spring tide: 22 December; neap tide: 30 December).

Model calibration focused on the bottom roughness length z_0, which was adjusted within 0.0001-0.003 m to reproduce surge processes; vertical mixing was computed with the Mellor-Yamada level-2.5 turbulence closure. Model performance was evaluated with the MAE, CC, and SS defined in Section 3.1, and the parameter set (z_0=0.0001 m) was used in the simulation.

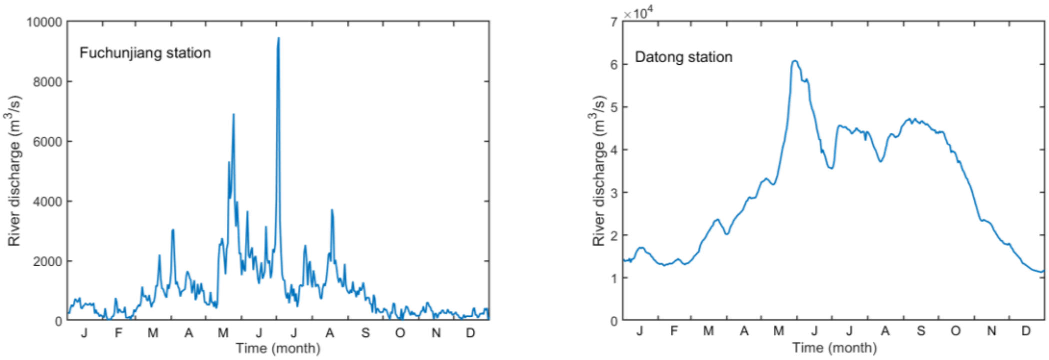

Fig. 2. Daily river discharge at the Fuchunjiang Hydropower Station and the Datong Station in 2021.

2.2. Salinity Stratification Parameters

The strength of freshwater-seawater mixing in the estuarine water column was evaluated using the stratification coefficient, defined as:

$$S_p = (S_b - S_s)/S_a \tag{1}$$

where S_b is the bottom salinity, S_s is the surface salinity, and S_a is the depth-averaged salinity. Following Prandle (1985), the water column is classified as strongly stratified when $S_p > 0.32$, well mixed when $S_p < 0.15$, and partially mixed or weakly stratified when $0.15 \leq S_p \leq 0.32$.

2.3. Salinity Front Identification

Salinity fronts in estuaries are characterized by rapid horizontal change in salinity across relatively short distances. The intensity and location of the salinity front can be quantified using the horizontal salinity gradient:

$$grad(S) = \Delta S/\Delta x \tag{2}$$

where ΔS denotes the salinity difference between two points and Δx represents the Euclidean distance between them. Based on field measurements reported by Hu et al. (1995), the horizontal salinity gradient within the Yangtze Diluted Water plume (salinity ~10-20 psu) is approximately 0.32 psu/nmi. The salinity boundary separating the two frontal systems in the HZB is defined as 13 psu (Su, 1992). Accordingly, in this study the two frontal zones are identified as follows: the QTR Plume Front is defined as the area with salinity < 13 psu and horizontal gradient exceeding 0.40 psu/nmi (0.22 psu/km), and the Secondary Front of the Yangtze Diluted Water is defined as the area with salinity ⩾ 13 psu and gradient surpassing 0.32 psu/nmi (0.17 psu/km). Using these criteria, the spatial distribution of frontal zones in the HZB was identified.

2.4. Residual Currents

The Eulerian residual current is defined as the mean velocity at a fixed location averaged over one or several tidal cycles (Rodríguez et al., 2017):

$$[\bar{u},\bar{v}] = \frac{1}{T}\cdot\int_{t_0}^{t_0+T}[u,v]\,dt \qquad (3)$$

where $u = u(t,x,y,z)$ and $v = v(t,x,y,z)$ represent the eastward and northward velocity components at time t, respectively, and $\overline{u}$ and $\overline{v}$ denote the corresponding Eulerian residual currents. Following Kong et al. (2007), a continuous 25-h dataset covering approximately two semidiurnal tidal cycles was selected to characterize the residual current in the HZB.

2.5. Wind stress curl and Ekman transport

Wind stress curl induces convergence or divergence of Ekman transport, which further modulates vertical ocean motions such as upwelling and downwelling. The corresponding formula is expressed as:

$$\tau_s = \rho_a C_D U|U| \qquad (4)$$

$$curl = \partial\tau_y/\partial x - \partial\tau_x/\partial y \qquad (5)$$

where τ_s denotes surface wind stress; τ_x is the eastward component of wind stress; τ_y is the northward component of wind stress; ρ_a represents air density, generally taken as 1.22 kg/m^3. C_D is the wind stress drag coefficient; and U refers to wind speed at 10 m above the sea surface.

The $curl$ positive values correspond to cyclonic wind stress curl, under which Ekman pumping drives the upward uplift of subsurface cold water and facilitates the formation of upwelling. In contrast, negative values represent anticyclonic wind stress curl, which pushes surface seawater downward and suppresses the development of upwelling.

The Ekman transport is calculated following the method proposed by Bakun (1973):

$$E = \tau_s/f\rho \qquad (6)$$

where ρ denotes seawater density, approximately 1025 kg/m^3; f is the Coriolis parameter.

3. Results

3.1. Model Validation

Model performance was evaluated using Mean Absolute Error (MAE), Correlation Coefficient (CC), and Skill Score (SS) (Warner et al., 2005).

3.1.1. Tide levels

Figure 3 presents tidal level time series at three monitoring stations (ZhenHai, SheShan, and ZhaPu), with error statistics summarized in Table 1. Forecast accuracy is high across all stations, with MAE values of 0.276 m, 0.131 m, and 0.252 m, respectively, demonstrating the model's capability to reproduce tidal processes. Observed and simulated amplitudes and phases of the dominant M_2 constituent are generally consistent. However, the model tends to slightly overestimate lowest water levels during certain tidal phases, consistent with findings reported by Li et al. (2024), likely reflecting residual discrepancies between interpolated and actual bathymetry at the grid scale. Overall, these results confirm that the hydrodynamic model performs well in reproducing tidal patterns.

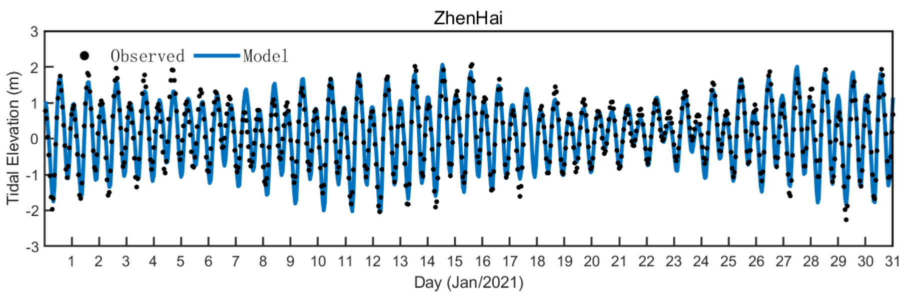

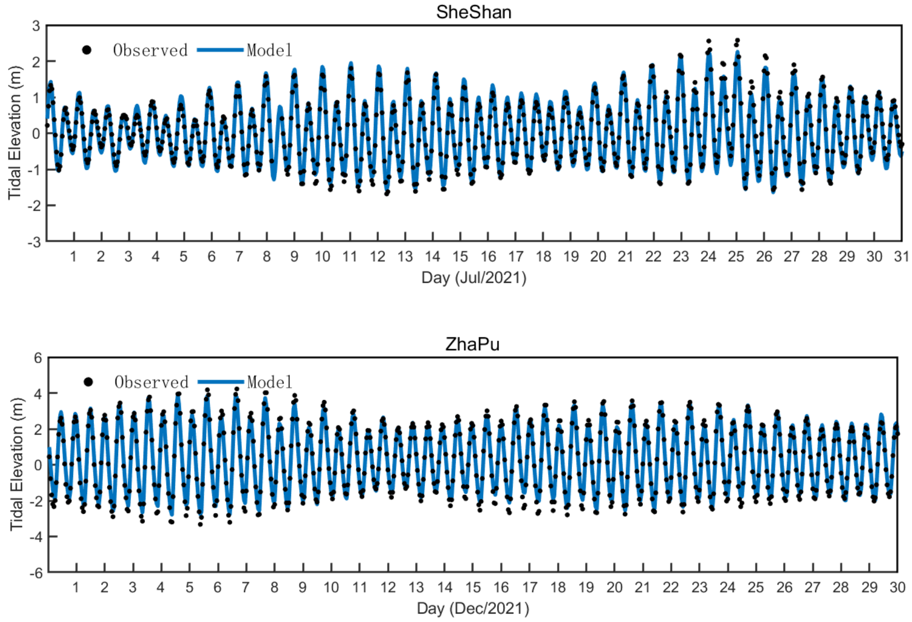

Fig. 3. Comparison between simulated and observed water levels in the HZB.

Table 1. Error statistics between modeled and observed water levels.

Station	Date	M_2		S_2		K_1		O_1		MAE/m
		|△A|/m	|△g|/°	|△A|/m	|△g|/°	|△A|/m	|△g|/°	|△A|/m	|△g|/°	
ZhenHai	Jan/2021	0.010	6.3	0.011	2.1	0.036	3.8	0.012	21.2	0.276
SheShan	Jul/2021	0.020	5.4	0.016	1.1	0.009	2.3	0.006	3.6	0.131
ZhaPu	Dec/2021	0.237	0.9	0.068	0.4	0.003	1.1	0.010	0.3	0.252

Note: A represents the amplitude, and g represents the lag angle.

3.1.2. Tidal Currents

A comparison of surface currents at monitoring stations in July and December 2021 (Fig. 4) demonstrates satisfactory overall simulation performance. The MAE of current velocity ranges from 0.13 to 0.32 m/s, with the CC ranging from 0.87 to 0.99 and SS between 0.85 and 0.94. For average current direction, MAE is less than 25°, the CC varies from 0.70 to 0.99, and the SS ranges from 0.84 to 0.99 (Table 2), indicating that the model effectively captures tidal current directions during both spring and neap tides. These results accurately reproduce tidal current structure under contrasting tidal conditions.

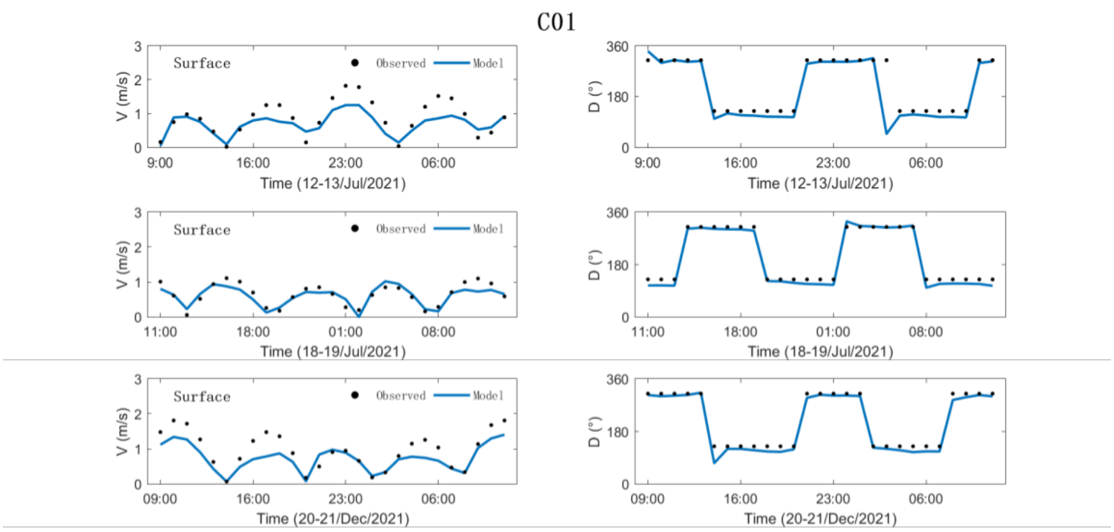

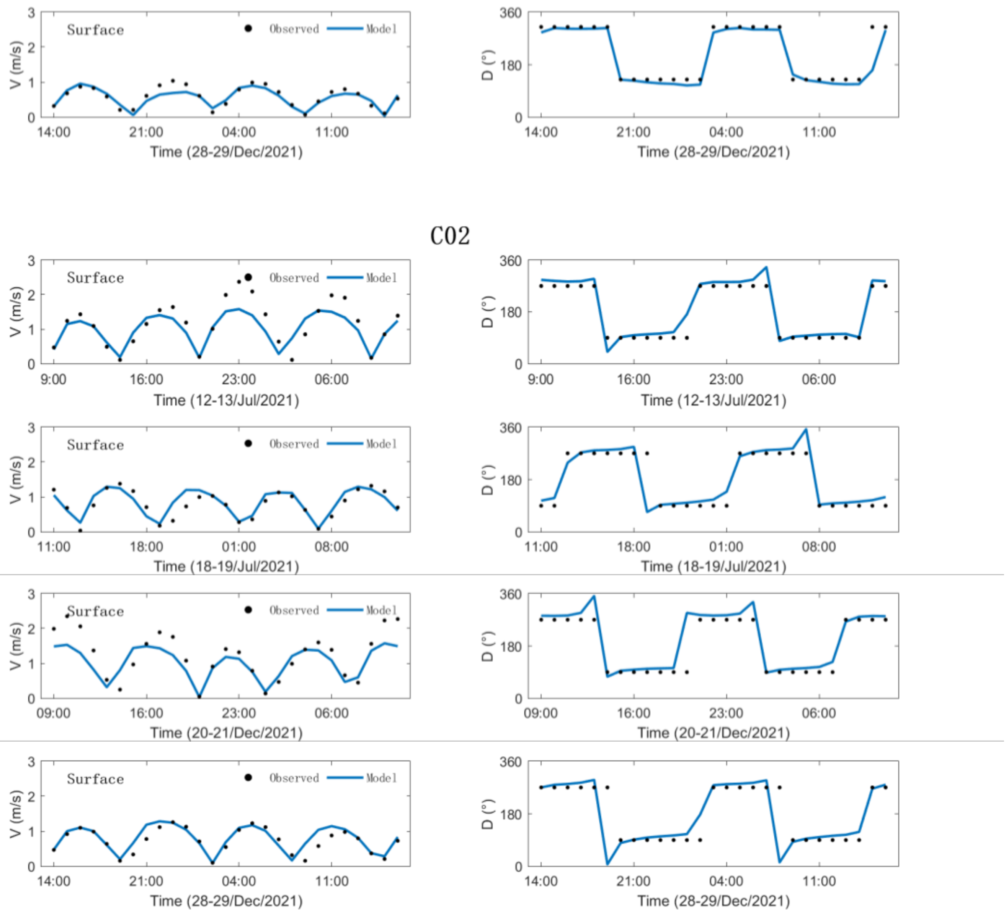

Fig. 4. Comparison between simulated and observed tidal currents in the HZB.

Table 2. Error statistics between modeled and observed tidal current.

Station		July 2021						December 2021					
		12-13/Jul/2021			18-19/Jul/2021			20-21/Dec/2021			28-29/Dec/2021		
		MAE	CC	SS	MAE	CC	SS	MAE	CC	SS	MAE	CC	SS
C01	V/(m/s)	0.25	0.90	0.85	0.13	0.87	0.92	0.25	0.91	0.87	0.10	0.90	0.94
	D/°	22.1	0.88	0.93	11.9	0.99	0.99	12.2	0.99	0.99	15.2	0.95	0.97
C02	V/(m/s)	0.26	0.88	0.89	0.14	0.88	0.93	0.32	0.87	0.86	0.12	0.88	0.93
	D/°	19.0	0.98	0.98	24.7	0.87	0.94	25.0	0.91	0.94	33.5	0.70	0.84
Average	V/(m/s)	0.25	-	-	0.13	-	-	0.28	-	-	0.11	-	-
	D/°	20.5	-	-	18.3	-	-	18.6	-	-	24.3	-	-

Note: V represents Tidal Current Velocity, D represents Tidal Current Direction.

3.1.3. Salinity

MAE between observed and modeled values at three stations ranged from 3.02 to 4.87 psu during the wet season and 2.40 to 6.32 psu during the dry season (Table 3). Considering the CC and SS together, CC values at all stations are generally higher in the wet season. BeiLun Station has a CC of 0.81, indicating excellent consistency between simulated and observed salinity variations. SheShan Station presents a high SS of 0.80 in the wet season, reflecting satisfactory overall model performance. The larger dry-season salinity errors, particularly the low SS at BeiLun (0.13), likely arise from uncertainties in the GLORYS open-boundary salinity, whose influence on the bay is amplified in the low-discharge season; the complex mixing between the Yangtze Diluted Water and shelf water north of the bay mouth; and unresolved small tributaries and local discharges along the southern shore. Although dry-season errors are slightly larger, overall fluctuation trends are consistent with observations (Fig. 5). The relatively high MAE at SheShan Station during the dry season reflects the influence of high-salinity offshore seawaters on the Yangtze Diluted Water plume north of the YRE, a region of complex mixing that is challenging to simulate precisely. Overall, the model reliably simulates the spatial distribution of estuarine salinity, with remaining errors attributable to the complex coastal morphology and strong hydrodynamic conditions in this region.

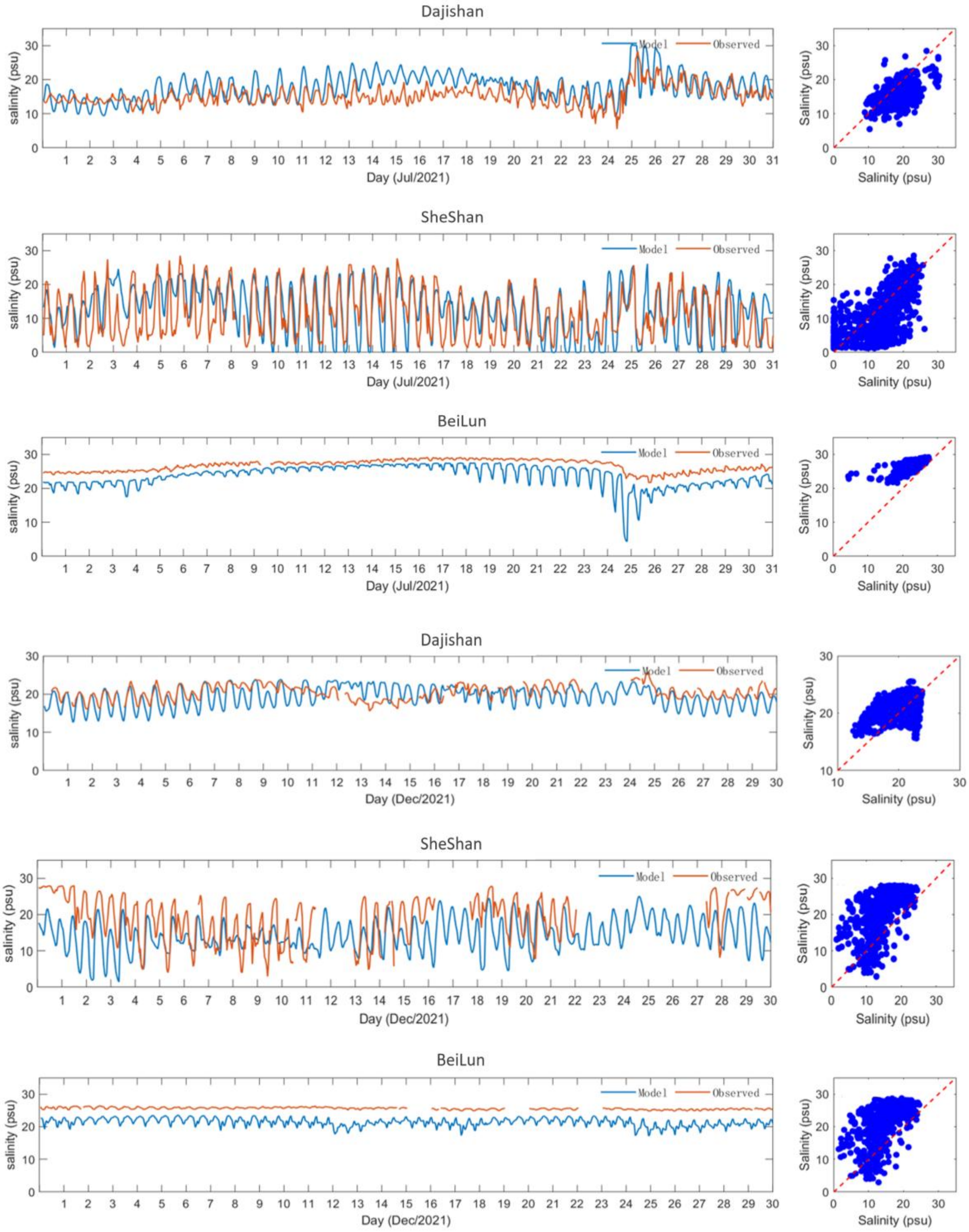

Fig. 5. Comparison between simulated and observed salinity in the HZB.

Table 3. Error statistics between modeled and observed salinity.

Station	Date	MAE	CC	SS
Dajishan	Jul/2021	3.41	0.51	0.64
	Dec/2021	2.40	0.35	0.57
Sheshan	Jul/2021	4.87	0.65	0.80
	Dec/2021	6.32	0.54	0.62
Beilun	Jul/2021	3.02	0.81	0.60
	Dec/2021	4.22	0.54	0.13

3.2. Spatiotemporal envelope of the HZB salinity fronts

Figure 6 illustrates the spatial distributions of surface salinity at four representative tidal stages during spring and neap tides in both the wet and dry seasons. Across all conditions, salinity contours exhibit a persistent northeast-southwest orientation, reflecting the combined influence of river discharge and offshore saline waters. Salinity is generally lower in the western and northern bay and higher in the eastern and southern regions, forming a robust cross-bay gradient structure.

During the wet season, enhanced freshwater discharge from both the QTR and the YR, together with the prevailing southeast monsoon, promotes the northeastward expansion of the Yangtze Diluted Water. Despite this expansion, the QTR plume remains dynamically significant, with the 10 psu isohaline extending seaward beyond the Nanhuizui. In contrast, during the dry season, reduced discharge from the QTR and YR, combined with intensified intrusion of high-salinity offshore water, lead to a landward migration of the 10 psu isohaline. Concurrently, strong northerly winds drive the Yangtze Diluted Water and coastal current southward, reinforcing the secondary plume front of the YR as it enters the HZB. Consequently, salinity near the bay mouth is generally lower in the wet season than in the dry season. Superimposed on these seasonal patterns, pronounced tidal variability is observed, with high-salinity waters intruding landward during flood tides and receding offshore during ebb tides.

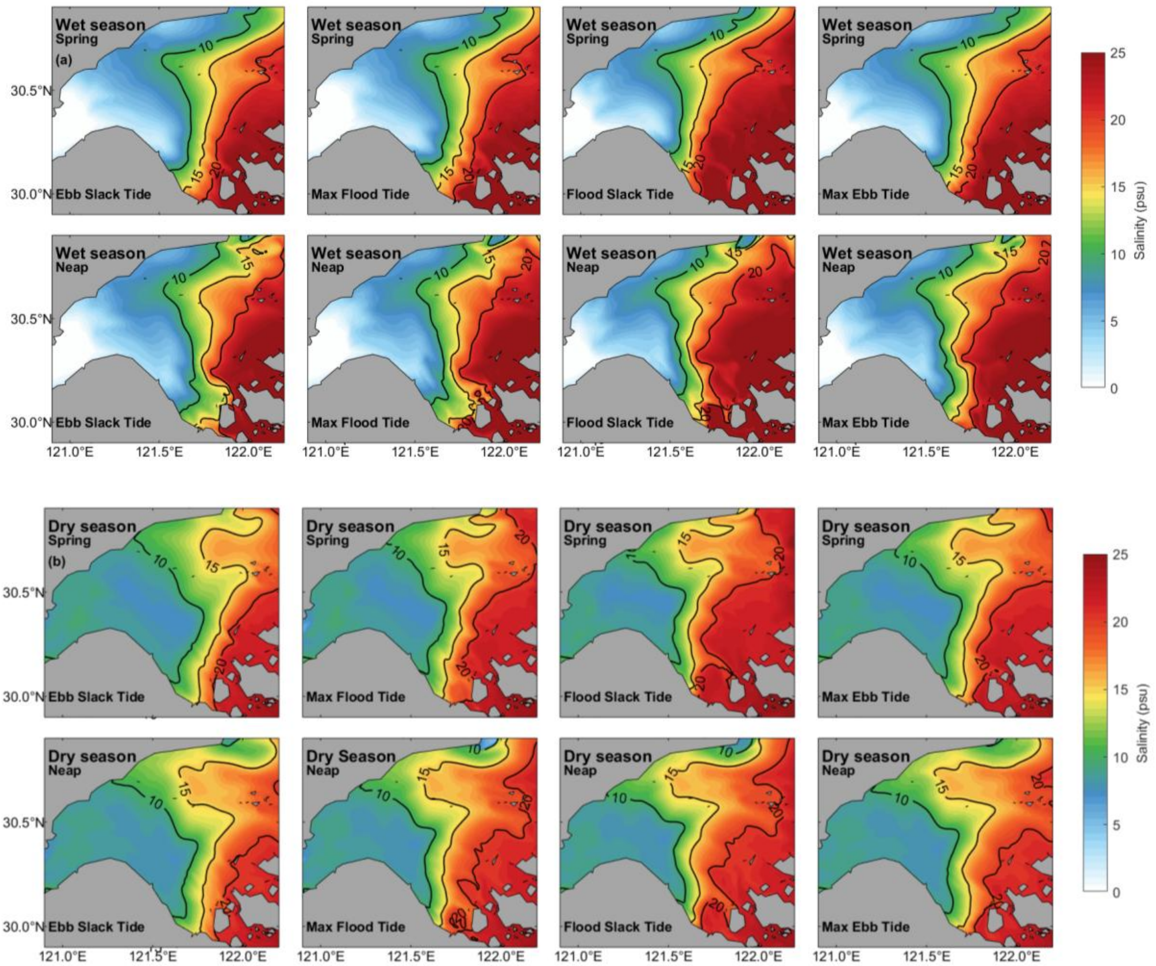

Fig. 6. Surface salinity distribution in the HZB under four tidal conditions during the wet and dry seasons.

Salinity fronts identified from horizontal salinity gradients consistently follow the NE-SW orientation in both seasons (Figs. 7(a) and 7(b)). During the wet season, a tongue-shaped frontal structure, referred to as the QTR Plume Front, extends from the GanPu-ZhaPu region toward the offshore area near Jinshanzui, with horizontal salinity gradient exceeding 0.22 psu/km. Additionally, a more intense frontal zone associated with the Yangtze Secondary Front is present in the outer bay, where salinity exceeds 13 psu. Notably, the overall frontal configuration remains relatively stable across different tidal phases during the wet season, indicating a persistent frontal framework.

In the dry season, frontal zones become narrower and markedly weaker, particularly in the southern HZB and around ZhaPu. The Secondary Front of the Yangtze Diluted Water appears more fragmented, while the QTR Plume Front loses its pronounced tongue-shaped structure and is expressed instead as a narrow, elongated frontal band. A clear divergence between the QTR Plume Front and the Yangtze Secondary Front is evident during this season. On average, frontal intensity in the wet season is approximately 5%-14% stronger than in the dry season. Frontal gradients are also systematically enhanced during neap tides compared to spring tides, with the maximum horizontal salinity gradient reaching ~0.89 psu/km during the max flood tide (Table 4).

Overall, despite pronounced seasonal and tidal modulations, the salinity fronts in HZB persist within a well-defined spatial domain and exhibit repeatable patterns of migration and intensity variability. These results demonstrate that the HZB salinity fronts evolve within a constrained spatiotemporal envelope, rather than exhibiting random or episodic behavior, thereby providing a robust basis for examining their vertical structure and associated circulation in the following sections.

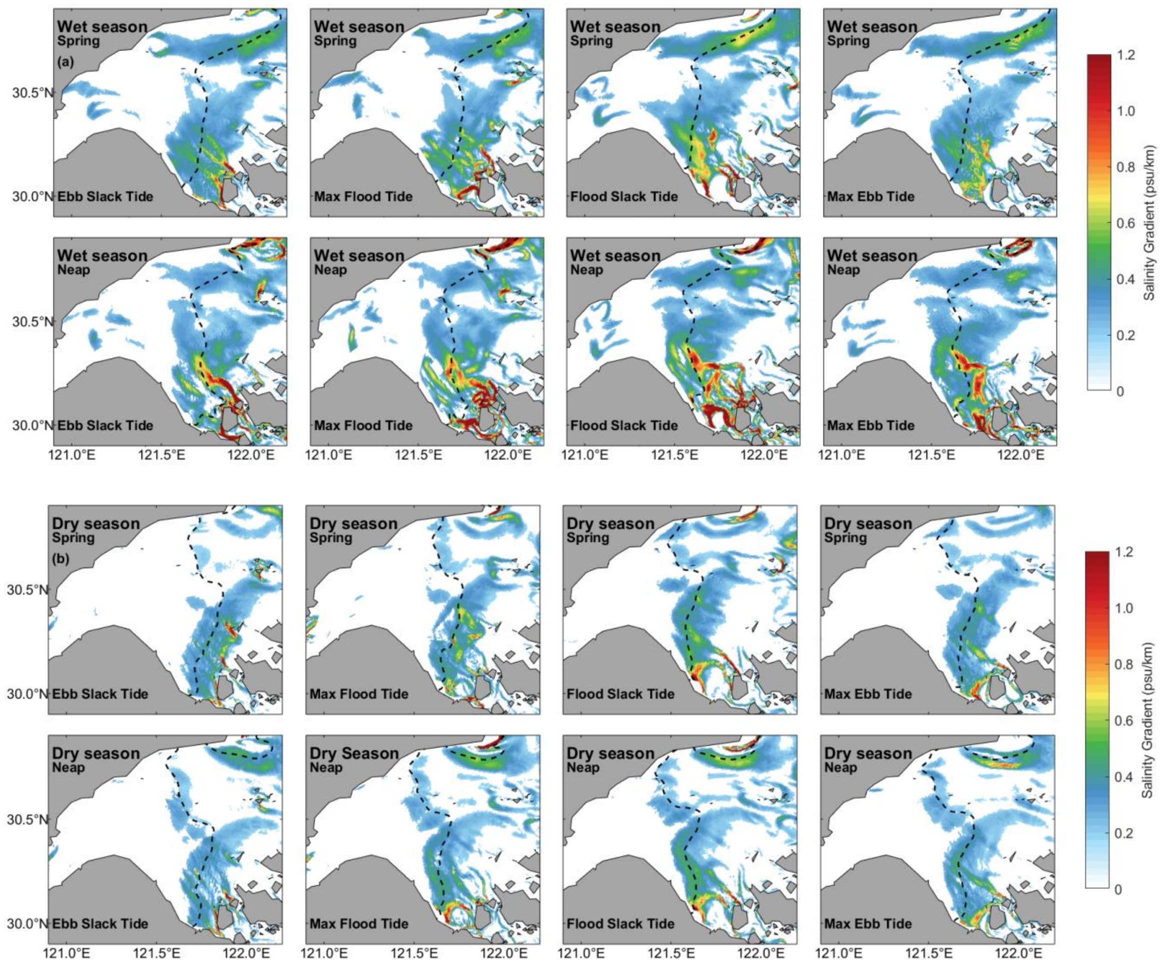

Fig. 7. Configuration of the surface salinity front in the HZB. The dashed line denotes the 13 psu isohaline; the shaded region indicates the spatial envelope within which the salinity front oscillates under different tidal and seasonal conditions.

Table 4. Mean surface horizontal salinity gradients in the HZB under different tidal and seasonal conditions (psu/km)

	Wet season				Dry season			
	Ebb slack	Max flood	Flood slack	Max ebb	Ebb slack	Max flood	Flood slack	Max ebb
Spring tide	0.68	0.73	0.74	0.66	0.64	0.73	0.70	0.61
Neap tide	0.81	0.89	0.88	0.77	0.66	0.85	0.81	0.63

3.3. Vertical asymmetry of the salinity front regulated by stratification

The salinity fronts in the HZB exhibit their most distinct vertical characteristics during flood tides, when the instantaneous structure of the water column and associated vertical motions are best preserved (Su, 1992). Accordingly, this section focuses on representative maximum flood tides to examine the vertical structure and evolution of the salinity fronts under different tidal and seasonal conditions.

During the wet season, the horizontal salinity gradient intensifies progressively from the surface toward the bottom, accompanied by a slight narrowing of the frontal width. This vertical enhancement of frontal intensity is particularly pronounced on the southern side of the front. Under neap tide conditions, this enhancement is most marked, indicating the strongest vertical asymmetry of the frontal structure. In contrast, during the dry season, the vertical differences in frontal intensity are much weaker, and the front exhibits a more vertically uniform structure (Fig. 8).

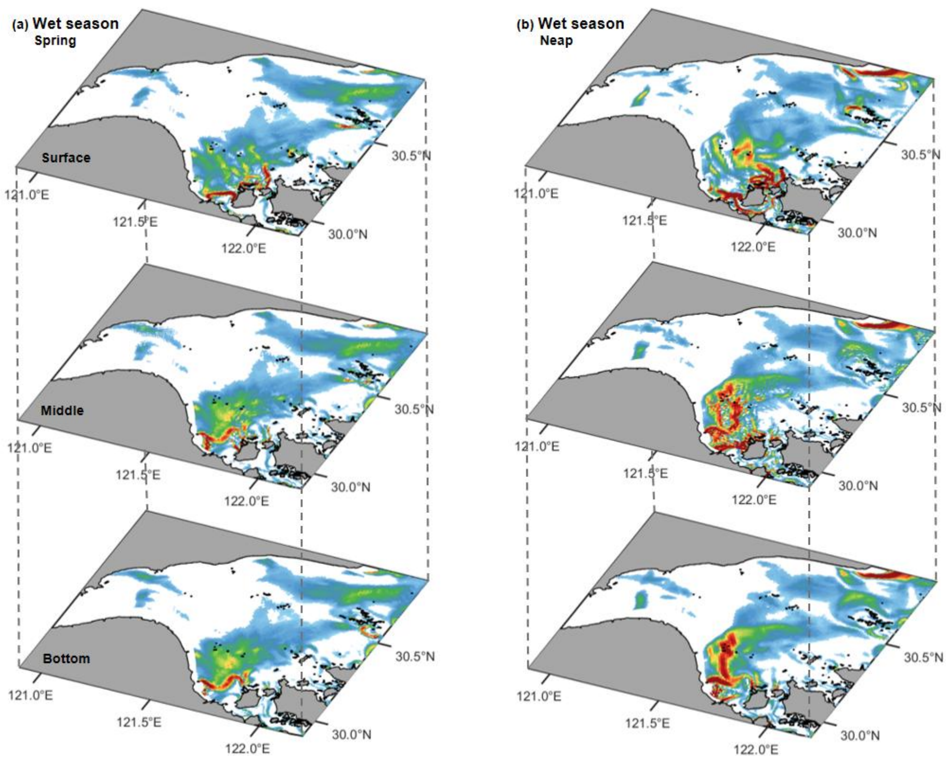

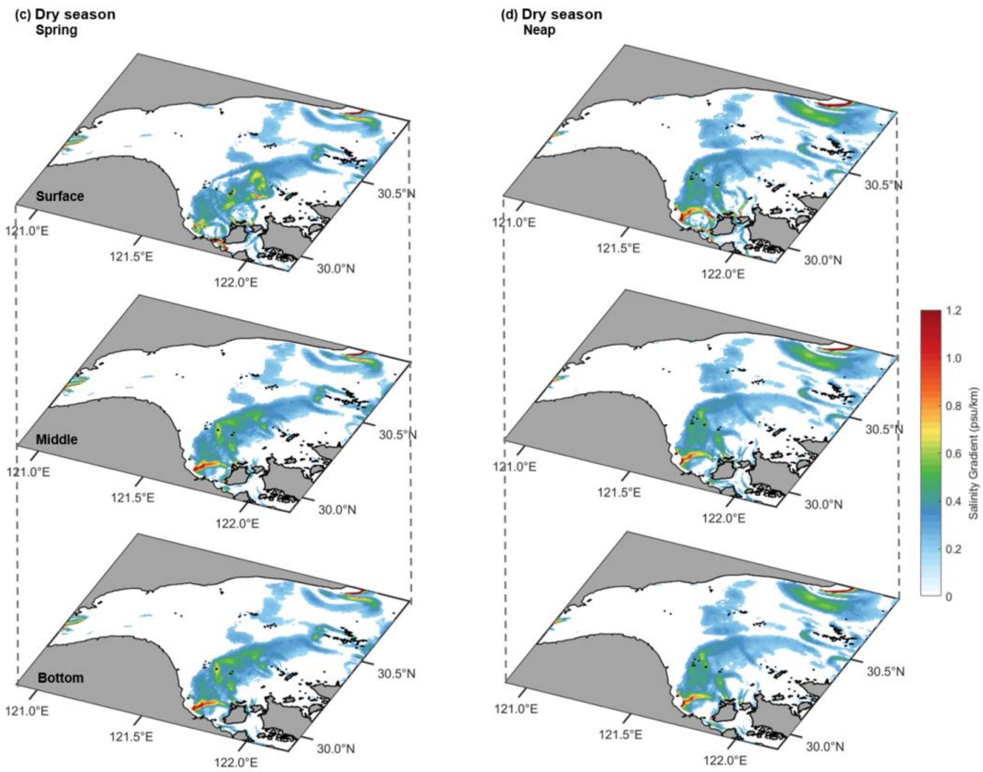

Fig. 8. Vertical salinity of the salinity front in the HZB under contrasting tidal and seasonal conditions, showing surface, middle, and bottom layers. Figures (a)-(d) correspond to spring tide in wet season, neap tide in wet season, spring tide in dry season and neap tide in dry season, respectively.

To further quantify the vertical asymmetry and stratification effects, two cross-front sections were selected based on horizontal salinity gradients and the 13 psu salinity threshold (Fig. 9). Cross-section 1 is located north of the bay mouth, offshore of the Nanhui Mouth, where the Yangtze Diluted Water enters the HZB. Cross-section 2 is situated on the southern side of the bay mouth and is oriented perpendicular to the 13 psu isohaline. A clear contrast in stratification is observed between the two sections. In cross-section 2, the surface-to-bottom salinity difference reaches up to 9 psu during the wet season and approximately 2 psu during the dry season. In comparison, cross-section 1 exhibits much weaker stratification, with maximum difference of approximately 3 psu in the wet season and 2.6 psu in the dry season. The strongest stratification occurs during the wet-season neap tide, reflecting the combined effects of enhanced freshwater input and reduced tidal kinetic energy.

Frontal positions along both sections were identified using the horizontal salinity gradient. During the wet season, the front in cross-section 1 is typically located 10-25 km from the shoreline, with maximum vertically averaged frontal intensity near 15 km (~1.13 psu/km during spring tide). In cross-section 2, the front spans a broader range (10-30 km from the shoreline), with salinity values of 4-23 psu. The maximum vertically averaged frontal intensity reaches ~1.35 psu/km near 10 km from the shoreline during neap tide. In the dry season, frontal intensity weakens and positions shift, with fronts occurring at 10-30 km in cross-section 1 and 8-20 km in cross-section 2.

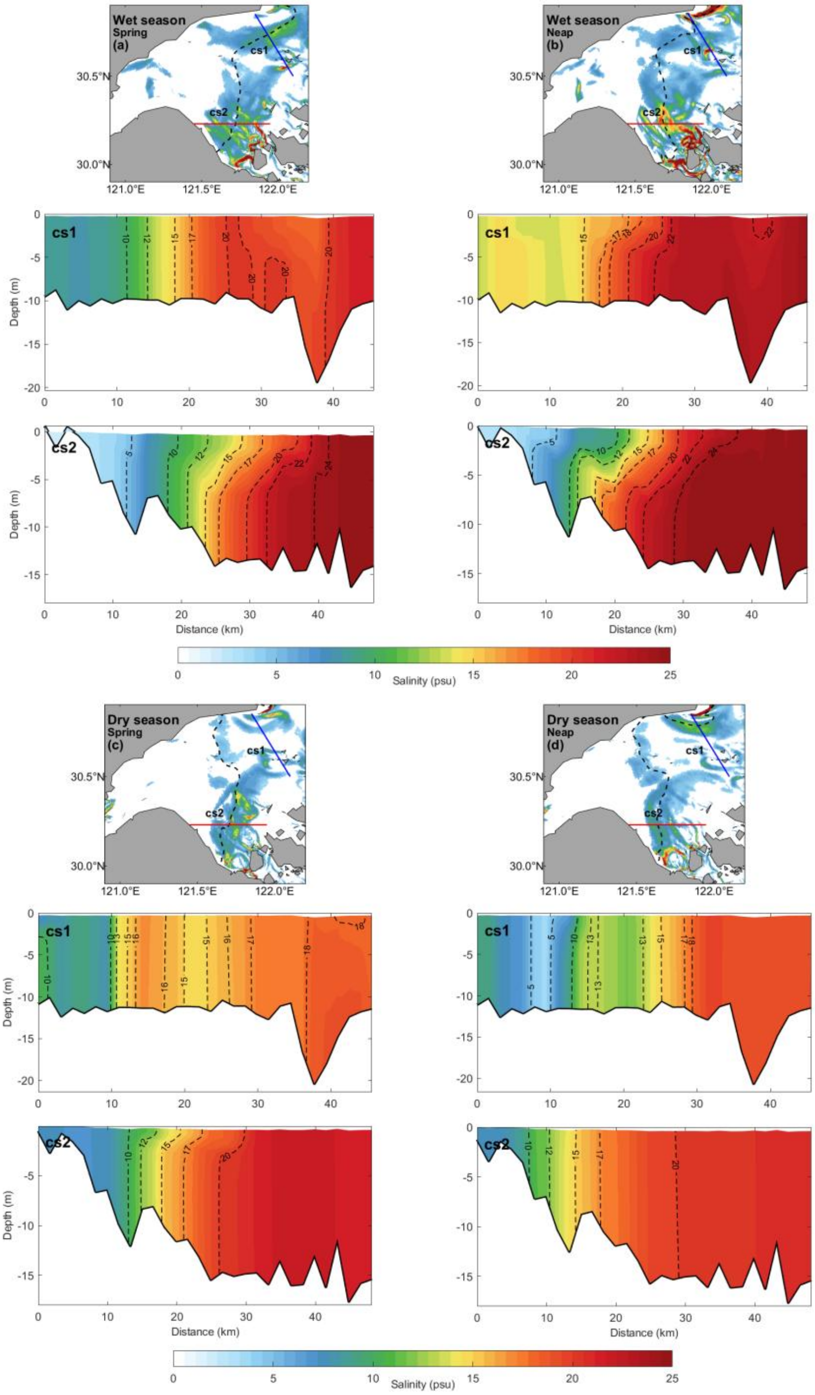

Fig. 9. Vertical salinity distribution along representative cross-section in the HZB. The section originates near the shoreline and extends seaward. Figures (a)-(d) correspond to spring tide in wet season, neap tide in wet season, spring tide in dry season and neap tide in dry season, respectively. The blue line cs1 and red line cs2 represent cross-section 1 and cross-section 2, while the black dashed lines denote salinity contours.

Salinity stratification parameters show a consistent pattern of increasing toward the frontal zone followed by a decrease downstream (Fig. 10). Peak values systematically coincide with frontal locations, where the water column is either partially mixed or stratified. Stratification parameters in cross-section 2 are significantly higher than those in cross-section 1 under all conditions. In cross-section 1, stratification values generally remain below 0.15, consistent with a well-mixed water column and a nearly vertical frontal structure. In contrast, cross-section 2 frequently exhibits stratification parameters exceeding 0.32 during the wet season, with maxima occurring at approximately 12, 20 and 26 km from the shoreline, corresponding closely to the frontal positions identified in Fig.

9.

During the wet-season neap tide, a pronounced double-peak pattern emerges in cross-section 2, with stratification parameters reaching 0.43 and 0.62 at distances of approximately 12 km and 20 km, respectively, indicating strongly stratified conditions and the development of an inclined frontal structure. The weakened tidal mixing during neap tides enhances salinity stratification, reinforcing the vertical separation between freshwater and saline water and intensifying horizontal salinity gradients. Consequently, surface-averaged frontal intensity reaches its maximum during these conditions. Similar behavior has been reported by Gong et al. (2018), who demonstrated that reduced mixing during neap tides can amplify baroclinic effects and strengthen estuarine circulation.

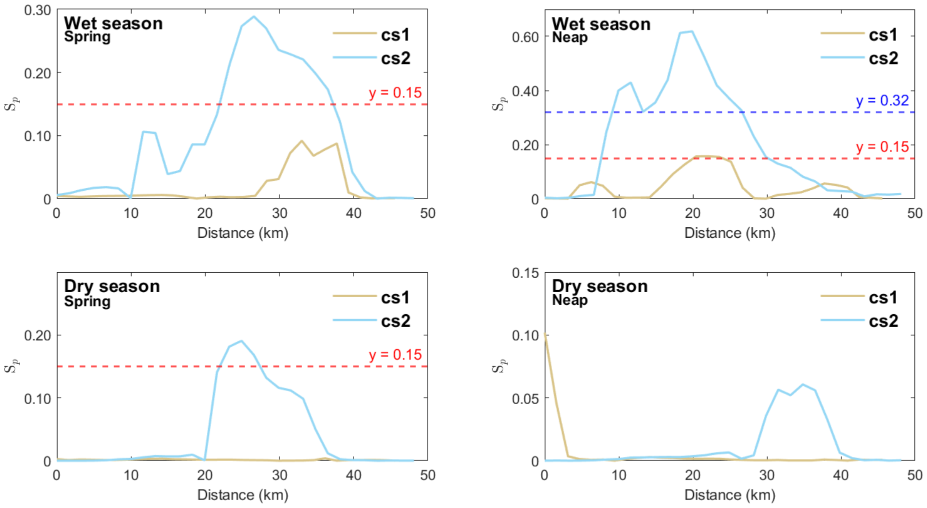

Fig. 10. Spatial distribution of the salinity stratification parameter along cross-sections in the HZB. The horizontal red dashed line marks the critical threshold of 0.15 for well-mixed water columns, and the horizontal blue dashed line denotes the critical threshold of 0.32 for strong stratification. cs1 and cs2 represent cross-section 1 and cross-section 2, respectively.

3.4. Front-locked circulation associated with the salinity front

The pronounced vertical asymmetry and stratification-dependent frontal structure described in Section 3.3 provide favorable conditions for the development of secondary circulation. Such frontal circulation plays a critical role in regulating cross-front exchange and material transport between contrasting water masses on either side of the salinity front.

The residual current was calculated based on the definition in Equation (3). Figure 11(a) illustrates surface and bottom residual current fields in the HZB under different tidal and seasonal conditions. During the wet season, residual current patterns exhibit pronounced tidal modulation: surface currents are predominantly northeastward during spring tides, whereas a distinct residual eddy develops in the central bay during neap tides. During the dry season, residual current directions show relatively minor variation with tidal phase; the surface layer generally displays a northeast-southeastward flow, while bottom currents are oriented northeast-northwestward, with a pronounced directional shift west of the Zhoushan Archipelago. Across all conditions, surface velocities consistently exceed bottom velocities, reaching maxima of approximately 20 cm/s near the bay head and along the southern side of the bay mouth, while velocity magnitudes in the central bay remain relatively uniform.

Vertical profiles of residual current (Fig. 11(b) and (c)) further reveal the front-locked nature of the circulation. Surface velocities typically range from 8 to 15 cm/s, whereas near-bottom velocities are weaker (5-8 cm/s). Notably, current speeds are reduced in the vicinity of the frontal zone, where vertical motions become more pronounced. In the frontal zone of cross-section 1, vertical velocities are on the order of 10^{-6}-10^{-5} m/s, while in cross-section 2 they reach 10^{-5} m/s, indicating strong vertical exchange on the southern side of the bay.

Distinct circulation patterns emerge across the two sections. In cross-section 1, residual currents are predominantly southeastward throughout the water column, with weak flow reversal near the bottom within the frontal zone, consistent with a relatively well-mixed water column and a near-vertical frontal configuration. In contrast, cross-section 2 exhibits clearly vertically sheared circulation: surface residual currents are directed seaward, while bottom currents flow landward across the front. This configuration gives rise to a clockwise circulation between 20-30 km from the shoreline, and another between 5-15 km during the wet-season neap tide. Importantly, the locations of these circulation structures closely coincide with regions of maximum salinity stratification identified in Section 3.3.

Overall, these results demonstrate that the residual circulation in the HZB is dynamically organized by the salinity front rather than being spatially uniform. The circulation strength, vertical structure, and spatial extent are strongly controlled by frontal stratification and tidal modulation, forming a coherent front-locked circulation system that provides a direct physical pathway for cross-front exchange and material transport.

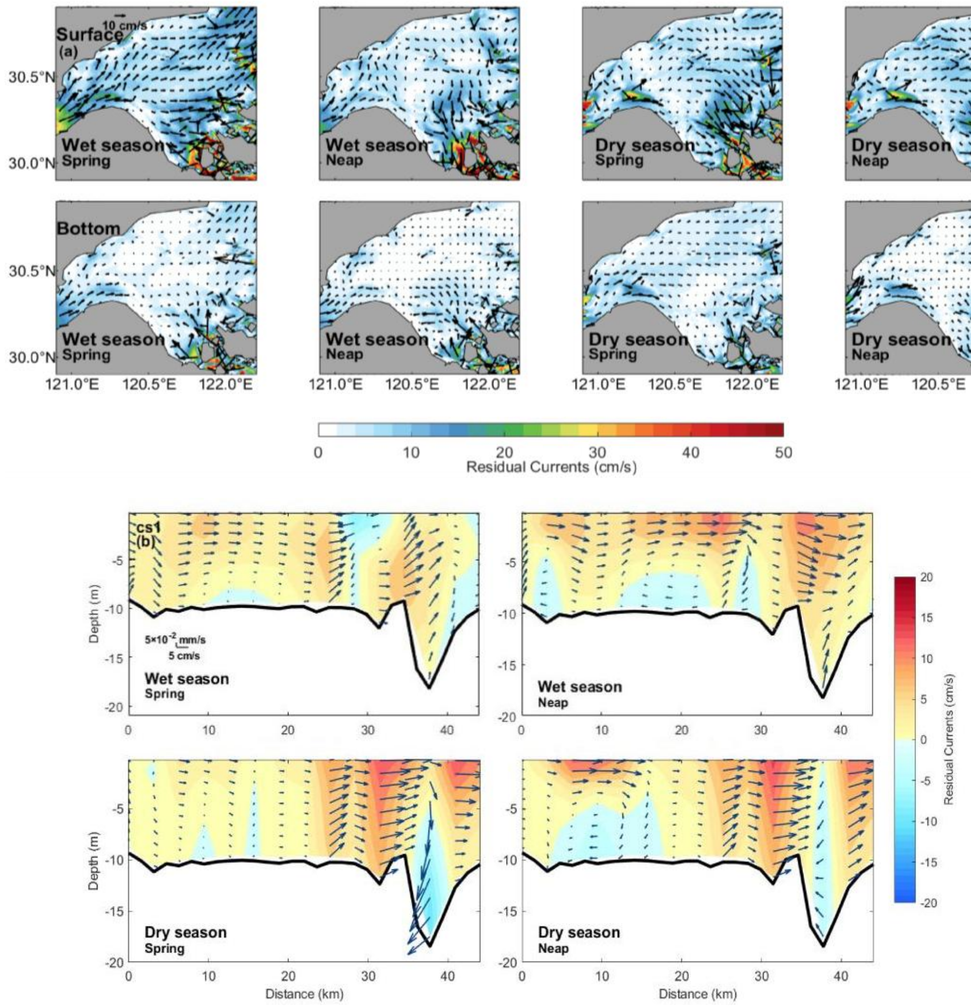

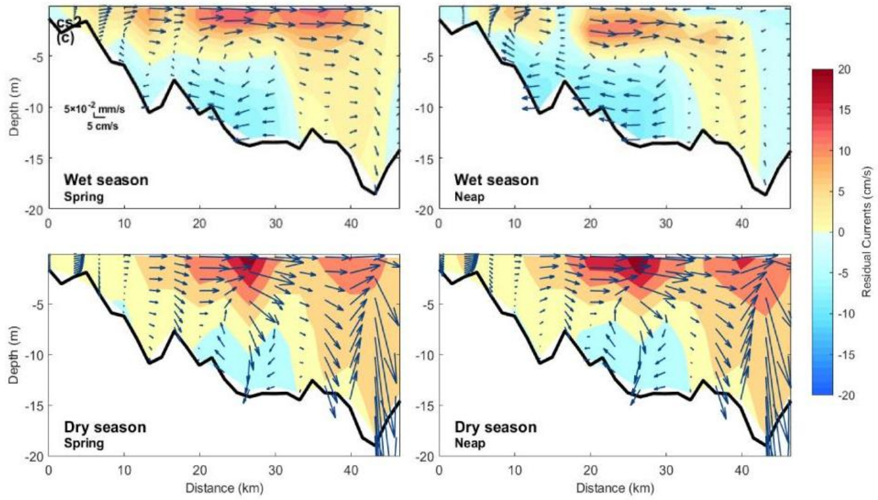

Fig. 11. Residual Current Field in the HZB. (a) Surface and bottom residual currents during spring and neap tides in the wet and dry seasons. (b) and (c) show the vertical residual current structure at selected cross-section 1 and cross-section 2, respectively; seaward direction is defined as positive.

4. Discussion

4.1. Primary dynamical balance governing the salinity front

The front-locked circulation identified in Section 3.4 provides a clear dynamical target for diagnosing the momentum balance that maintains the salinity front in the HZB. Using momentum diagnostics derived from the high-resolution three-dimensional FVCOM simulation, we examine the dominant forces governing the residual circulation.

The *x*-component momentum equation referenced from Chen et al. (2006) is expressed as:

$$\frac{\partial u}{\partial t}+u\frac{\partial u}{\partial x}+v\frac{\partial u}{\partial y}+w\frac{\partial u}{\partial z}-fv = -\frac{1}{\rho_0}\frac{\partial P}{\partial x}+\frac{\partial}{\partial z}\left(K_m\frac{\partial u}{\partial z}\right)+F_u \qquad (7)$$

where K_m stands for the vertical eddy viscosity coefficient, and F_u represents the horizontal momentum diffusion term. The first term on the right-hand side of the equation is the *x*-direction pressure gradient force. The second term on the right-hand side of the equation is the vertical mixing term, which embodies the contribution of wind stress at the surface and bottom friction near the bed.

Diagnostic analysis of the along-transect momentum equation indicates that residual circulation associated with the salinity front is primarily governed by the baroclinic balance (Fig. 12). Across both seasonal and tidal conditions, the baroclinic pressure gradient arising from horizontal density contrasts is the fundamental driver of the frontal circulation (Chen et al., 2025), while bottom friction and the Coriolis force play critical roles in regulating its vertical structure and magnitude. The spring-neap modulation of stratification (strongest during wet-season neap tides) explains the observed spring-neap contrast in frontal intensity through the competition between tidal mixing and baroclinic forcing. The role of neap-tide stratification in amplifying baroclinic effects is discussed in relation to the mechanism reported by Gong et al. (2018).

A pronounced asymmetry in the momentum balance is evident between the surface and bottom layers. Near the surface, residual currents are relatively strong and are influenced by pressure gradients and, episodically, by wind stress. Near the bottom, circulation is consistently dominated by bottom friction and the Coriolis force, leading to weaker velocities and frequent flow reversal relative to the surface. This balance produces a vertically sheared circulation structure, particularly intensified within the frontal zone, and explains why bottom currents are persistently weaker than surface currents across all examined conditions.

Seasonal variations in river discharge strongly modulate this balance by altering vertical stratification. During the wet season, enhanced freshwater input increases density stratification, suppresses vertical mixing, and strengthens baroclinic pressure gradients, intensifying frontal circulation and salinity gradients, especially during neap tides when tidal mixing is weakest. In contrast, reduced runoff during the dry season weakens stratification and diminishes the baroclinic forcing, making the maintenance more reliant on the combined effects of weak tidal mixing and episodic wind forcing.

Comparisons with other estuarine systems highlight the distinct dynamical regime of the HZB. While wind stress and pressure gradient forces dominate the momentum balance in systems such as the Pearl River Estuary (Zheng et al., 2014) and Tampa Bay (Chen et al., 2019), bottom circulation in the HZB remains consistently controlled by bottom friction and Coriolis effects under all seasonal and tidal conditions. The stratification-controlled vertical asymmetry is discussed in relation to partially mixed systems such as northern San Francisco Bay (Monismith et al., 2002), the Hudson River estuary (Scully et al., 2009), and macrotidal partly-mixed estuaries (Uncles and Stephens, 1990), and the frontogenesis mechanism is related to Corlett and Geyer (2020) and Chen et al. (2025). This persistent frictional control reflects the macrotidal nature of the HZB and contributes to the robust vertical shear and front-locked circulation observed in the frontal zone.

Overall, the momentum diagnostics demonstrate that the salinity front in the HZB is primarily sustained under a frictionally modified baroclinic balance, with its intensity jointly modulated by seasonal river discharge variability, tidal mixing intensity, and wind forcing. This dynamical framework accounts for the spring-neap disparities in frontal strength observed in our simulations. Nevertheless, wind forcing can impose substantial short-term modulation on the surface frontal circulation, highlighting the considerable independent influence of wind effects that will be elaborated in the next section.

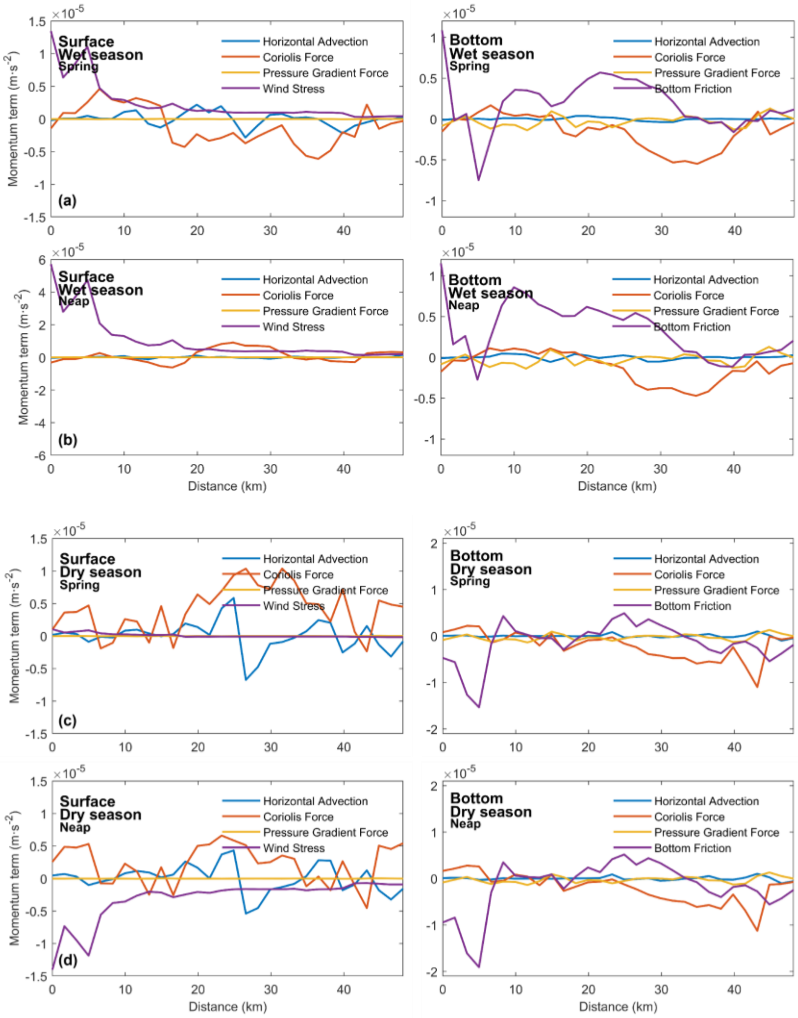

Fig. 12. Momentum diagnosis of the surface and bottom layer circulation along cross-section 2 in the HZB. Figure

(a)-(d) illustrate the hydrodynamic fields at the surface and bottom layers under four scenarios: spring tide in wet season, neap tide in wet season, spring tide in dry season, and neap tide in dry season.

4.2. Wind-induced modulation of the salinity front

While the primary dynamical balance maintaining the salinity front in the HZB is governed by a frictionally modified baroclinic balance (Section 4.1), wind forcing acts as an important secondary mechanism that modulates frontal structure and circulation on seasonal and synoptic timescales. Through its influence on surface transport, stratification, and coastal upwelling or downwelling, wind forcing can enhance or weaken the horizontal salinity gradient and adjust frontal position (Walker et al., 2005; Moon et al., 2009; Zhang and Hu, 2021; Lao et al., 2023; Nampoothiri et al., 2024).

Wind stress curl was calculated and seasonal wind characteristics were analyzed based on Equations (4)-(6). The regional wind field over the HZB exhibits a pronounced seasonal reversal: northerly to northeasterly winds dominate from November to March (dry season), whereas southeasterly winds prevail from April to August (wet season). Correspondingly, wind stress curl over the southern HZB transitions from negative values in winter to positive values in spring and summer, reaching a maximum in July before weakening again in autumn (Fig. 13(a)). This seasonal evolution exerts strong control on Ekman pumping and the direction of Ekman transport (Fig. 13(b)).

During the wet season, southeasterly winds induce offshore Ekman transport along the Zhejiang coast. Combined with positive wind stress curl, this configuration favors Ekman upwelling of high-salinity bottom water in the nearshore region. The wind-driven upwelling acts in concert with enhanced river discharge to increase vertical stratification and strengthen baroclinic pressure gradients, thereby intensifying the horizontal salinity gradient and frontal strength. This mechanism helps explain why salinity fronts in the HZB are systematically stronger during the wet season than the dry season (Table 4). In contrast, during the dry season, prevailing northerly winds drive onshore Ekman transport associated with negative wind stress curl, suppressing coastal upwelling of high-salinity water. Although northerly winds facilitate the southward advection of Yangtze Diluted Water into the bay, the substantially reduced river discharge weakens stratification and diminishes baroclinic forcing, resulting in markedly weaker horizontal salinity gradient and frontal intensity.

Overall, wind forcing in the HZB does not fundamentally generate the salinity front but systematically modulates its intensity, position, and associated circulation. This secondary but significant wind modulation, acting together with runoff variability and tidal mixing, reinforces the seasonal contrast in frontal strength and provides an additional pathway for variability superimposed on the primary baroclinic-frictional balance.

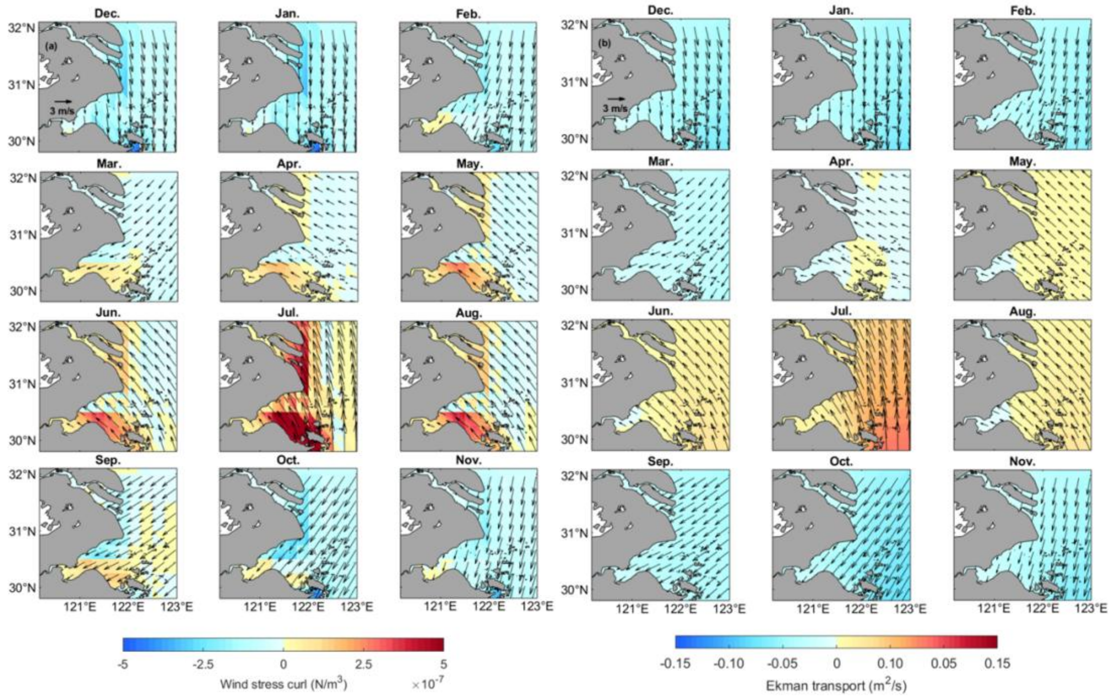

Fig. 13. Spatial distributions of wind stress curl and surface wind field, together with Ekman transport in the HZB and adjacent coastal waters from 1940 to 2021. Positive Ekman transport indicates offshore transport; negative values indicate onshore transport.

4.3. A process-based conceptual framework for macrotidal estuarine salinity fronts

Early studies of frontal systems in the HZB relied primarily on field observations and identified salinity fronts using fixed horizontal salinity gradient thresholds (e.g., >0.4 or ≥0.3 psu/nmi) (Su, 1992). While these criteria provided a useful first-order description, they cannot adequately capture the spatiotemporal variability of salinity fronts across different tidal regimes and seasons. By integrating high-resolution three-dimensional numerical simulations with frontal diagnostics, stratification metrics, and momentum balance analyses, the present study moves beyond fixed-gradient definitions and proposes a process-based conceptual framework for HZB salinity fronts in macrotidal estuaries (Fig. 14).

A key feature of this framework is the pronounced spatial contrast in frontal structure within the HZB. North of the bay mouth, persistently strong tidal mixing maintains well-mixed conditions across virtually all tidal and seasonal regimes, producing a near-vertical frontal structure with relatively weak vertical shear. By contrast, the southern part of the bay is characterized by partially mixed to stratified conditions, where frontal structure is highly sensitive to variations in river discharge and tidal mixing, and gently inclined to strongly slanted frontal configurations develop, accompanied by intensified baroclinic circulation and front-locked secondary flows.

The framework further explains the contrasting behavior of salinity fronts under different tidal regimes. During the wet season, enhanced river discharge strengthens vertical stratification, particularly during neap tides when tidal mixing is weakest, leading to stronger horizontal salinity gradients and intensified frontal circulation. This process-based interpretation accounts for the finding that frontal intensity is generally higher during neap tides than during spring tides in the present study, contrasting with observations from the early 1990s, when different hydrological and morphological conditions prevailed. During the dry season, reduced runoff weakens stratification and promotes more mixing; nevertheless, northerly winds during neap tides can partially compensate for the reduced baroclinicity by modulating surface transport and frontal position, thereby contributing to frontal maintenance.

This conceptual framework is constructed based on the validated high-resolution three-dimensional characterization of the salinity front in the HZB under contrasting seasonal and tidal conditions. By integrating frontal diagnostics, stratification metrics and momentum balance analysis, it enables the quantitative interpretation of dynamic mechanisms that could only be qualitatively described in previous observation-based and two-dimensional studies. This method holds the potential to be transferred to frontal research in other macrotidal estuaries. Nevertheless, several limitations remain in the present study. Although the framework performs well under representative seasonal-tidal conditions, its quantitative extrapolation is constrained. Further sensitivity experiments are required to explore the influences of interannual variability, bathymetric effects and extreme conditions. Meanwhile, comparative analyses of diverse macrotidal estuaries should be conducted to further verify the general applicability of this framework to other systems.

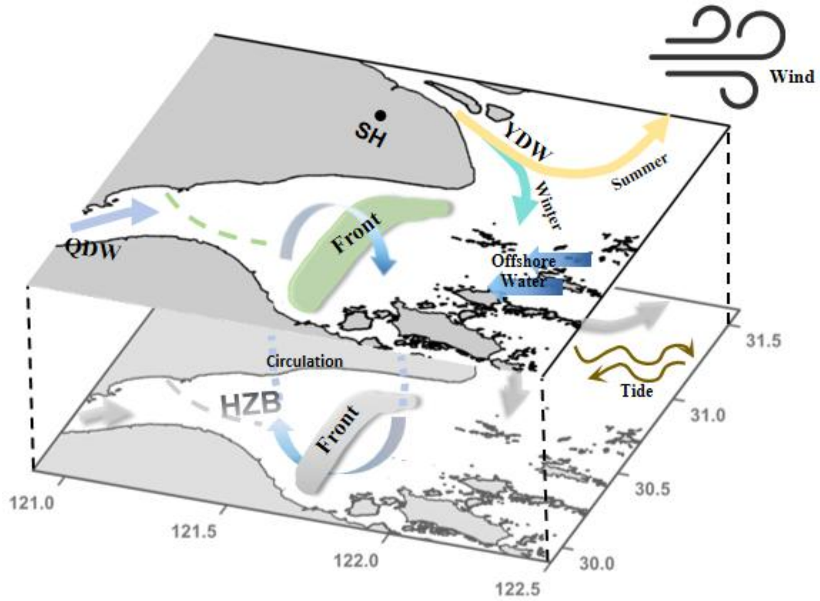

Fig. 14. Schematic representation of salinity front structure in the HZB. QDW and YDW denote the Qiantang River Diluted Water and Yangtze River Diluted Water, respectively. The dashed line indicates the frontal configuration during the wet season; the others represent the year-round persistent frontal structure.

5. Conclusions

Using a high-resolution FVCOM hydrodynamic model, this study investigated the spatiotemporal variability, vertical structure, and circulation dynamics of salinity fronts in the HZB under contrasting seasonal and tidal conditions. The main conclusions are as follows:

(1) The HZB salinity front is a persistent but dynamically modulated feature driven by the interplay of the QTR discharge, offshore high-salinity waters, and the Yangtze River Diluted Water. Frontal morphology and intensity exhibit pronounced seasonal and tidal variability: the front is more coherent and stronger during the wet season, reflecting enhanced stratification and baroclinic forcing; frontal intensity is slightly greater during neap tides than during spring tides, owing to reduced tidal mixing and enhanced stratification, with wind-induced modulation providing an additional contribution.

(2) Salinity stratification exhibits strong spatial variability across the bay. North of the bay mouth, the water column remains well-mixed under most conditions, resulting in a near-vertical frontal structure. In contrast, the southern part of the bay is characterized by partially mixed to strongly stratified conditions during wet-season neap tides, highlighting the critical role of runoff-tidal interaction in regulating vertical frontal asymmetry.

(3) The salinity front is associated with a coherent, front-locked circulation rather than a spatially uniform residual flow. Surface residual currents are generally stronger than bottom currents across all seasons, with maxima near the bay entrance. The southern frontal zone supports stronger vertical motions and well-defined single or double circulation cells, whereas circulation in the northern frontal zone is weaker, consistent with its

well-mixed water column structure.

(4) Momentum diagnostics demonstrate that the salinity front and its associated circulation are maintained by a frictionally modified baroclinic balance. Baroclinic pressure gradients provide the primary driving force, while bottom friction and the Coriolis force regulate the vertical shear and suppress bottom currents within the frontal zone. Wind forcing acts as a secondary modulator, enhancing or weakening frontal intensity by influencing stratification, surface transport, and coastal upwelling or downwelling, especially during neap tides.

In summary, this study establishes a process-based understanding of salinity fronts in a macrotidal estuarine system, emphasizing the coupled roles of discharge variability, tidal mixing, stratification and frictional dynamics. The process-based framework developed here advances the mechanistic understanding of estuarine frontal dynamics and provides a scientific basis for regional ecological conservation, port management, and marine environmental forecasting.

CRediT authorship contribution statement

Jiawei Zhang: Formal analysis, Methodology, Validation, Visuali zation, Writing – original draft. Jingui Liu: Conceptualization, Funding acquisition, Project administration, Writing – review & editing. Shuo Li: Data curation, Writing – review & editing. Shunqi Pan: Supervision, Writing – review & editing.

Declaration of competing interests

The authors declare that they have no known competing financial interests or personal relationships that could have appeared to influence the work reported in this paper.

Acknowledgement

This study was supported by the Project of Key Laboratory of Ocean Space Resource Management Technology, MNR (Grant NO. KF-2023- 109).

Data availability

Data will be made available on request

References

Bakun, A., 1973. Coastal upwelling indices, west coast of North America. Washington, DC: United States Government Printing Office.

Belkin, I. M., Cornillon, P. C., Sherman, K., 2009. Fronts in large marine ecosystems. Prog. Oceanogr. 81(1–4), 223–236.

Cardoso, P. G., 2022. Estuaries: dynamics, biodiversity, and impacts. In Life Below Water. Cham: Springer International Publishing, pp. 355–366.

Chen, C., Beardsley, R. C., Cowles, G., 2006. An unstructured grid, finite-volume coastal ocean model (FVCOM) system. Oceanography. 19(1), 78–89.

Cromwell, T., Reid, J.L. Jr., 1956. A study of oceanic fronts. Tellus 8 (1), 94–101.

Chen, J., Weisberg, R. H., Zheng, L., Hu, C., Zhang, Y., Nickerson, A. K., Donovan, J., Liu, Y., 2025. Frontogenesis by material convergence in an estuary and its adjacent coastal ocean. Limnol. Oceanogr. 71, 1 – 17.

Chen, J., Weisberg, R. H., Liu, Y., Zheng, L., Zhu, J., 2019. On the momentum balance of Tampa Bay. J. Geophys. Res., Oceans. 124(7), 4492–4510.

Corlett, W. B., Geyer, W. R., 2020. Frontogenesis at estuarine junctions. Estuar. Coast. 43, 722–738.

Du, P., Ding, P., Hu, K., 2010. Simulation of three-dimensional cohesive sediment transport in Hangzhou Bay, China. Acta Oceanol. Sin. 29, 98–106.

Ferrari, R., 2011. A frontal challenge for climate models. Sci. 332(6027), 316–317.

Gong, W. P., Lin, Z. Y., Chen, Y. Z., Chen, Z. Y., Zhang, H., 2018. Effect of winds and waves on salt intrusion in the Pearl River estuary. Ocean Sci. 14(1), 139–159.

Hickox, R., Belkin, I., Cornillon, P., Shan, Z. Q., 2000. Climatology and seasonal variability of ocean fronts in the East China, Yellow and Bohai Seas from satellite SST data. Geophys. Res. Lett. 27(18), 2945–2948.

Hu, F., Hu, H., Gu, G., 1995. Salinity fronts in the Changjiang river estuary. Oceanol. Limnol. Sin. (S1), 23–31.

Huang, D. J., 1993. On the front-induced current structure in shallow sea. Oceanol. Limnol. Sin. 24(4), 385–392.

Kong, Y. Z., Ding, P. X., He, S. L., 2007. Analysis of basic characteristics of residual current in the Changjiang River estuary and adjacent sea areas. Adv. Mar. Sci. 25(4), 367–375.

Lao, Q., Liu, S., Ling, Z., Jin, G., Chen, F., Chen, C., Zhu, Q., 2023. External dynamic mechanisms controlling the periodic offshore blooms in Beibu Gulf. J. Geophys. Res. Oceans. 128(6), e2023JC019689.

Lévy, M., Franks, P. J. S., Smith, K. S., 2018. The role of submesoscale currents in structuring marine ecosystems. Nat. Commun. 9, 4758.

Li, L., Wu, L., Chen, X., Ren, Y., Ye, T., Yang, M., Zhao, X., 2024. Asymmetric tidal dynamics in the macro-tidal Hangzhou Bay, China. Estuar. Coast. 47(6), 1418–1434.

Li, Y., Yang, E., Pan, Y., Gao, Y., 2022. Numerical modeling of the impact of sea level rise on tidal asymmetry in Hangzhou Bay. J. Mar. Sci. Eng. 10(10), 1445.

Liu, D. Y., Lü, T., Lin, L., Wei, Q. S., 2022. Review of fronts and its ecological effects in the shelf sea of China. Advances in Marine Science. 40(4), 725–741 (in Chinese with English abstract).

Lohmann, R., Belkin, I. M., 2014. Organic pollutants and ocean fronts across the Atlantic Ocean: a review. Prog. Oceanogr. 128, 172 – 184.

Miller, P. I., Christodoulou, S., 2014. Frequent locations of oceanic fronts as an indicator of pelagic diversity: application to marine protected areas and renewables. Mar. Policy. 45, 318–329.

Monismith, S. G., Kimmerer, W., Burau, J. R., Stacey, M. T., 2002. Structure and flow-induced variability of the subtidal salinity field in northern San Francisco Bay. J. Phys. Oceanogr. 32(11), 3003–3019.

Moon, J.-H., Hirose, N., Yoon, J.-H., 2009. Comparison of wind and tidal contributions to seasonal circulation of the Yellow Sea. J. Geophys. Res., Oceans. 114(C8), C08025.

Nampoothiri, S. V. N., Sudheesh, V., Bepari, K. F., Reddy, B. B., K, N., K, R., Vijayan, A. K., Gupta, G. V. M., 2024. Formation mechanisms and biogeochemical response of coastal salinity front in the central eastern Arabian Sea. Dyn. Atmos. Oceans. 108, 101498.

Ning, X. R., Shi, J. X., Cai, Y. M., Liu, C. G., 2004. Biological productivity front in the Changjiang Estuary and the Hangzhou Bay and its ecological effects. Haiyang Xuebao. 26(6), 96–106 (in Chinese with English abstract).

Prandle, D., 1985. On salinity regimes and the vertical structure of residual flows in narrow tidal estuaries. Estuar. Coast. Shelf Sci. 20(5), 615–635.

Rodríguez, P. A., Carbajal, N., Rodríguez, J. H. G., 2017. Lagrangian trajectories, residual currents and rectification process in the Northern Gulf of California. Estuar. Coast. Shelf Sci. 194, 263–275.

Scanes, P., Ferguson, A., Potts, J., 2017. Estuary form and function: implications for palaeoecological studies. In Applications of paleoenvironmental techniques in estuarine studies. Dordrecht: Springer Netherlands, pp. 9–44.

Scully, M. E., Geyer, W. R., Lerczak, J. A., 2009. The influence of lateral advection on the residual estuarine circulation: A numerical modeling study of the Hudson River estuary. J. Phys. Oceanogr. 39(1), 107–124.

Su, J. L., 1992. Research on the Hangzhou Bay Front. In Oceanography in China. Beijing: Ocean Press (in Chinese).

Tian, Q., Wang, Y. P., Zhu, J. R., Li, W. H., 2025. Simulated characteristics of estuarine fronts in the Changjiang River Delta. J. Oceanol. Limnol. 43(3), 692–708.

Uncles, R. J., Stephens, J. A., 1990. The structure of vertical current profiles in a macrotidal, partly-mixed estuary. Estuar. Coasts. 13(4), 349–361.

Walker, N. D., Wiseman, W. J., Rouse, L. J., Babin, A., 2005. Effects of river discharge, wind stress, and slope eddies on circulation and the satellite-observed structure of the Mississippi River plume. J. Coast. Res. 21(6), 1228–1244.

Wang, N., Li, K., Song, D., Bi, N., Bao, X., Liang, S., Li, G., 2024. Impact of tidal shear fronts on terrigenous sediment transport in the Yellow River Mouth: Observations and a synthesis. Mar. Geol. 469, 107222.

Wang, T., Zhao, S., Zhu, L., McWilliams, J. C., Galgani, L., Amin, R. M., Nakajima, R., Jiang, W., Chen, M., 2022. Accumulation, transformation and transport of microplastics in estuarine fronts. Nat. Rev. Earth Environ. 3(11), 795–805.

Wang, X., Shi, X., Wang, G., Qiao, S., Liu, T., 2013. Sedimentation rates and its indication to distribution of Yangtze sediment supply around the Yangtze (Changjiang) River Estuary and its adjacent area, China. Earth Sci. J. China Univ. Geosci. 38(4), 763–775.

Warner, J. C., Geyer, W. R., & Lerczak, J. A., 2005. Numerical modeling of an estuary: a comprehensive skill assessment. J. Geophys. Res. Oceans. 110(C5), 1–13.

Xu, Y., Wang, Y., Zhan, L., Ou, Y., Jia, K., Mao, M., Zhu, X., Jiang, Z., Zhu, Y., Huang, W., Du, P., Zeng, J., Shuo, L., Zhou, F., 2024. Salinity fronts shape spatial patterns in Zooplankton distribution in Hangzhou Bay. Acta Oceanol. Sin. 43(6), 96 – 106.

Zhang, Y., Hu, C., 2021. Ocean temperature and color frontal zones in the Gulf of Mexico: Where, when, and why. J. Geophys. Res. Oceans. 126(10), e2021JC017544.

Zheng, S., Guan, W., Cai, S., Wei, X., Huang, D., 2014. A model study of the effects of river discharges and interannual variation of winds on the plume front in winter in Pearl River Estuary. Cont. Shelf Res. 73, 31–40.